Novel assessment of in-operations mapped stainless steel elbow pipe internal wall for detection of corrosion and scale deposition

A.K. Hamzat,[1]* A.M. Memon[2] and L.M. Alhems[1,2]

[1]*Department of Mechanical Engineering, King Fahd University of Petroleum and Minerals, Dhahran 31261, Saudi Arabia*
[2]*Applied Research Center for Metrology, Standards, and Testing (ARC-MST), Research Institute, King Fahd University of Petroleum and Minerals, Dhahran 31261, Saudi Arabia*
**E-mail: g201706110@kfupm.edu.sa*

Abstract

Corrosion and deposition of scale onto the pipelines pose a great risk in the petroleum industry. If proper detection and monitoring techniques are not employed, scale deposits can lead to a reduction of flow area as well as obstruction of entire sections in pipeline infrastructure. In this work, ultrasonic testing, visual inspection, and spectroscopic techniques have been combined to investigate the influence of simulated seawater on corrosion and scale deposition on 316L stainless steel elbow. Specifically, ultrasonic thickness gauge was used externally to study the changes in wall thickness of the elbow pipe, which was then visually inspected using a borehole camera. To characterize the morphology and composition of the scale deposit, a sample was extracted and characterized using scanning electron microscopy (SEM), energy-dispersive X-ray spectroscopy (EDS), X-ray diffraction (XRD), X-ray fluorescence (XRF), and Fourier transform infrared spectroscopy (FT-IR). Scales accumulation on the pipe internal wall prompted a slight increase in the wall thickness before cleaning and a maximum decrease of 14% after cleaning. The extracted scale sample characterization reveals the formation of $CaCO_3$ scale of the Aragonite phase and is traced to the composition of the simulated seawater. Multiple techniques deployments for assessment of corrosion and scale deposition in elbow help stop both processes and ultimately assist in the oil and gas industry.

Received: March 30, 2022. Published: October 18, 2022 doi: 10.17675/2305-6894-2022-11-4-5

Keywords: *simulated seawater, stainless steel, corrosion and scale monitoring, calcium carbonate scale, ultrasonic testing.*

1. Introduction

Corrosion and scale deposition are the two most persistent and expensive problems in oil and gas industries. Corrodible surfaces are found in many locations such as pipe walls, valves, casing flow lines, heater treaters, downhole equipment, pumps, and other production equipment and facilities [1]. Scale is defined as the deposition of an organic and inorganic compound on surface when local saturated limit is exceeded. Formation of mineral deposits in oilfield can lead to an emergency shutdown, loss of system efficiency, damage in the reservoir, flow accelerated corrosion, and premature equipment replacement. The economic

implication of scale deposits can be very serious due to high maintenance and equipment replacement costs [2–4]. The costs associated with scale were estimated at USD 9 billion in the United States, USD 3 billion in Japan, and USD 0.8 billion in Great Britain [5]. The evolution of scale deposits on equipment surfaces retards the efficient operation of the system, thus necessitating a detailed understanding of scale formation and its effective control. Another characteristic of scale formation is that the deposit can act as a protection for pipe wall against corrosive medium. Apart from the blockage of oil pipeline, scale formation leads to fouling in heat exchanger and HVAC equipment thereby reducing the heat transfer efficiency [6].

Scale formation in oil and gas fields is a complex chemical process influenced by many factors such as incompatible water, temperature [7], pressure [8], pH [9], flow velocity [10], and presence of salt or metal ions [11]. Quddus and Al-Hadrami reported that the scale deposition rate in pipes is strongly affected by the solution hydrodynamics [12]. Similarly, Müller-Steinhagen revealed that fouling resistance reduced at lower flow velocities [13]. The most common types of scales encountered in oil industry are carbonates, *e.g.*, $CaCO_3$ and $FeCO_3$, which are noticed at the early stages of oil extraction process, and sulfates, *e.g.*, $CaSO_4$, $SrSO_4$, and $BaSO_4$, which are prevalent at later stages. Foreign materials like corrosion products, weld points on the metal surface, or small suspended solid particles are the root cause of scale deposition on solid surfaces (*e.g.*, pipelines) [14]. The source of these foreign materials is hard to trace thereby making scale formation on the solid surface difficult to understand and predict. Owing to this, there is a need for establishing how such materials are deposited so as to devise prevention and control strategies [15, 16].

Several techniques are employed to detect and monitor scale in pipelines. These methods can be broadly classified into intrusive and non-intrusive. Formers interfere with the operation of equipment and are unsuitable for real-time inspection of pipelines. However, later can be used for real-time assessment of scale in pipelines without interference with the operation. Typical examples of intrusive scale detection methods are visual inspection, and analysis of the scale material using scanning electron microscope (SEM), atomic force microscopy (AFM), membrane properties analysis, to name a few. Ultrasonic guide waves, magnetic flux leakage (MFL), radiography, and infrared thermography are typical examples of non-intrusive methods.

The success of scale removal in oilfield depends largely on scale monitoring and detection techniques adopted. Scale formations have been investigated by several researchers using available strategies. Kippersund *et al.* monitored the formation of a solid depositon the pipe using ultrasonic guide waves [18]. They conducted experiments to detect the onset of hydrate formation by attenuation measurement over multiple loads. The results demonstrated an early detection of the onset of hydrate formation. Furthermore, a comparison with temperature increase in pipe confirmed the feasibility of obtaining deposit thickness information from bi-layer modes. Smith *et al.* introduced novel techniques for the detection of onset and evolution of calcium carbonate scale deposition in the West Texas oil field [19]. Attenuated total reflectance (ATR) probe was used to obtain the information about

scale formation at an early stage. The field test results revealed that the ATR scale sensor is not affected by crude oil, suspension solid, and any other foreign materials and can detect the severity of $CaCO_3$ scaling. However, the new sensor was unable to differentiate scale types (*e.g*., calcite, gypsum, barite, *etc*.)

A real-time technique was proposed by Poyet *et al.* for the detection of scale deposition and determination of its composition and thickness in oilfield tubing and pipe [20]. Their method was based on the energy gamma-ray attenuation measurements at an oil field. This novel method was reported to allow easy detection and characterization of the scale at an early stage of its formation without flow disruption. In a similar study, Jelbuldina *et al.* designed and fabricated carbon nanotubes (CNTs) based field-effect transistor (FET) for NaCl scale detection in the oilfield [21]. They deposited and integrated CNTs film with an FET like device adopting inkjet printing method in their study. The design sensor device showed a high response to chloride scale with a sensitivity of 8.6 towards a 3% NaCl solution. Rostron critically reviewed all the literature available on scale detection strategies [22]. The author compared different methods in addition to their benefits as well as limitations and recommended a novel non-destructive method that can detect and identify early stages of scale formation in the pipelines to address the gap in reviewed literature. Early detection of deposit formation in the pipes helps to develop an effective amelioration strategy which underlines the importance of adopting a real-time nondestructive technique for scale detection and monitoring in oil and gas industries.

Oliveira *et al.* characterized the scale deposit sample extracted from blocked oil pipes using X-Ray microfluorescence (Micro-XRF) and X-Ray microtomography (microCT) [23]. They analyzed the elemental and structural composition of the scale deposit sample, revealed different types of scales based on the elemental distribution (predominantly $CaCO_3$ and $BaSO_4$), and how they were deposited inside the pipes. The results obtained from both techniques provided data for optimization of the scale deposit prevention and removal methods. In a similar work, Singh characterized the scale deposit sample collected from choked oil production pipeline of the Arabian Gulf region oil field [24]. Results showed that the most commonly found scales in the region are calcium carbonate ($CaCO_3$), barium sulfate ($BaSO_4$), strontium sulfate ($SrSO_4$) and calcium sulfate ($CaSO_4$). Deposit formation in a water distribution system was characterized by Echeverría *et al.* [25], using energy dispersive spectroscopy (EDS), X-ray diffraction (XRD), infrared spectroscopy (IR), and scanning electron microscopy (SEM). Their result revealed that aluminosilicate, tubercles, and calcite are the main deposits at various sites of the water distribution system. In a related study, Cui *et al.* characterized the corrosion scale extracted from a 304 stainless steel delivery pipe in a reclaimed water system in service for 12 years to reveal the morphology and chemical composition of stainless steel corrosion scale and corroded passive film [26]. Three spectroscopic equipment (Raman spectroscopy (RMS), X-ray photoelectron spectroscopy (XPS), X-ray fluorescence spectrometer (XRF)) was used for characterization. The results revealed that the corrosion scale is mainly composed of hematite, goethite, magnetite, lepidocrocite, siderite, ferrous oxide, chromium green and chromite. Corrosion

product composition was identified as podiform chromite originating from localized corrosion region.

Scale deposit sample collected from 20 drinking water distribution systems (DWDSs) in the United States was analyzed to obtain the elemental and structural composition [27]. The wet scales were obtained from the unlined cast pipe, dried in an oven at 103°C for 24 hours, crushed and sieved before characterize using XRD and SEM. The major constituent element of the scale was Iron, followed by other elements in a decreasing order: Sulphur, organic carbon, calcium, inorganic carbon, phosphorus, manganese, magnesium, aluminum, and zinc. The XRD spectrum showed that goethite (α-FeOOH), magnetite (Fe_3O_4) and siderite ($FeCO_3$) were the primary crystalline phases identified in most of the samples. The deposit formed on the evaporator unit of a sugar factory in New South Wales, Australia was characterized using XRD and SEM by Peng *et al.* [27]. The result revealed the composition of the fouled deposit which varied with the tube height. The innermost layer attached to the tube wall contained amorphous silica, hydroxyapatite and organic matter as the prevalent elements, while amorphous silica, calcium oxalate dehydrate, and organic matter were the major elements found on the outermost layer surface.

Olufade and Simonson used both intrusive and non-intrusive methods to study the evolution of crystallization fouling in heat and membrane exchanger, and HVAC application [28]. Membranes were fouled in a 12h test in which $MgCl_{2(aq.)}$ was dehydrated in a liquid-to-air membrane exchanger at two operating conditions, low and high fouling rates, and characterized to identify the structure and composition of the deposit. SEM micrograph of the crystal deposit confirmed the octahedral shape $MgCl_2 \cdot 6H_2O$ while the energy-dispersive X-ray spectroscopy (EDX) analysis revealed that the main elements of crystal deposit were Mg, Cl, and O. Apart from altering the internal cross-section of the pipe, scale formation also influences the corrosion behavior of the pipe material by altering the morphology and physicochemical properties of the surface layers. Influence of $CaCO_3$ scale on the corrosion behavior of carbon steel was reported in [10, 29–33]. Their studies provide a unique approach for simultaneous monitoring of scale formation and corrosion in various environments, therefore, enabling the development of an inhibitor. Also, an appreciable increase in scale thickness and corrosion rate with increase in flow velocity was reported.

As seen from the above literatures, scale deposit formation in pipes is influenced by many factors and can be detected by various methods. However, to the best of authors' knowledge, there is a lack of studies in the area of scale formation in stainless steel elbows, where high scale formation rate is expected due to the sudden change in the flow direction. Also, available methods for scale detection and monitoring in pipes have limitations and there is a need to address those shortcomings. It is very difficult to predict the scaling condition in the internal walls of the elbow pipe. Application of ultrasonic internal inspection tools can help to address this; however, they do not provide information about the composition and structure of the detected deposit. Incorporation of both ultrasonic tools and spectroscopic analysis can provide useful information about the scaling status and its impact on the pipe's internal walls.

This paper addresses aforementioned gap through the application of both intrusive (spectroscopy and visual inspection using pipeline endoscope) and non-intrusive (ultrasonic wall-thickness gauge or UT) methods to detect and characterize the scale deposited in a stainless steel elbow, where UT provided the information about the amount of scale in terms of change in pipe's wall thickness, while spectroscopic methods, such as scanning electron microscope - energy dispersive X-ray spectroscopy (SEM-EDS), Fourier transform infrared spectroscopy (FT-IR), X-ray diffractometer (XRD), and X-ray fluorescence (XRF), gave the composition and structure of the scale deposit sample.

2. Experimental

Experiments were performed in a state of the art mini-flow loop that was designed and assembled in Multiphase Laboratory of King Fahd University of Petroleum and Minerals (KFUPM), Dhahran, Saudi Arabia. The flow loop was designed to simulate real-time industrial conditions and carry out detailed experimental investigations. This system is kept in an area providing a safe location for researchers to monitor and detect the formation of scale as well as the effect of single parametric change on the scale formation rate of the specimen. The schematic diagram and photograph of the mini flow loop are shown in Figure 1. It consists of PVC pipes, two centrifugal pumps from Lowara Company, model #TG334, flow rate (Q) 45 m^3/h, head (h) 110 m, OMEGA turbine flow meter (FTB730), power switch (Eurotherm 2500P Schneider Electric), Plexiglass pipe section, and elbow section of 316L stainless steel with composition in wt.% shown in Table 1. Plexiglass was installed at the exit arm of the elbow pipe to visually monitor the flow condition.

Preliminary runs of the simulated seawater through the system at three different salinities, 30‰, 35‰, and 40‰, revealed that the most aggressive environment exists at 35‰ salinity. This underlined the reason for using this value of salinity for the experiment. To evaluate the impact of simulated seawater on corrosion and scale deposit in the pipe elbow, 35 kg pure dried vacuum (PDV) salt was dissolved in 1 m^3 of tap water and agitated well using a paddle mixer. Handheld refractometer (REF234) was used to measure the salinity of the prepared solution which was kept at 35 ppt to mirror natural seawater with properties shown in Table 2. The fluid was supplied from a 2 m^3 storage tank and circulated using both centrifugal pumps which gave a maximum combined flow rate of 70 m^3/hr. Control valves were used to regulate the flow rates at the pump entrance and exit. The rates and total flow pumped was measured using an inline turbine flow meter. Stainless steel elbow was 3.01 m long with 4 in. internal diameter and a nominal wall thickness of 6.03 mm. The flow inlet and outlet arms of the elbow were 1.2 and 1.25 m long (including 0.6 m long Plexiglass), respectively. Inlet arm, elbow section, and outlet arm of the pipe elbow are all made of corrosion resistant 316 L stainless steel.

Before the experiment, ultrasonic thickness (UT) gauge (Elcometer: MTG8DL) was used to measure pipe elbow wall thickness to get the baseline values with which subsequent measurements were compared. The storage tank was rinsed thoroughly with distilled water and filled with the simulated seawater. The pumps were used concurrently and maximum

operating flow rate of 70 m^3/hr equivalent to Reynold number of approx. 100,000 was achieved.

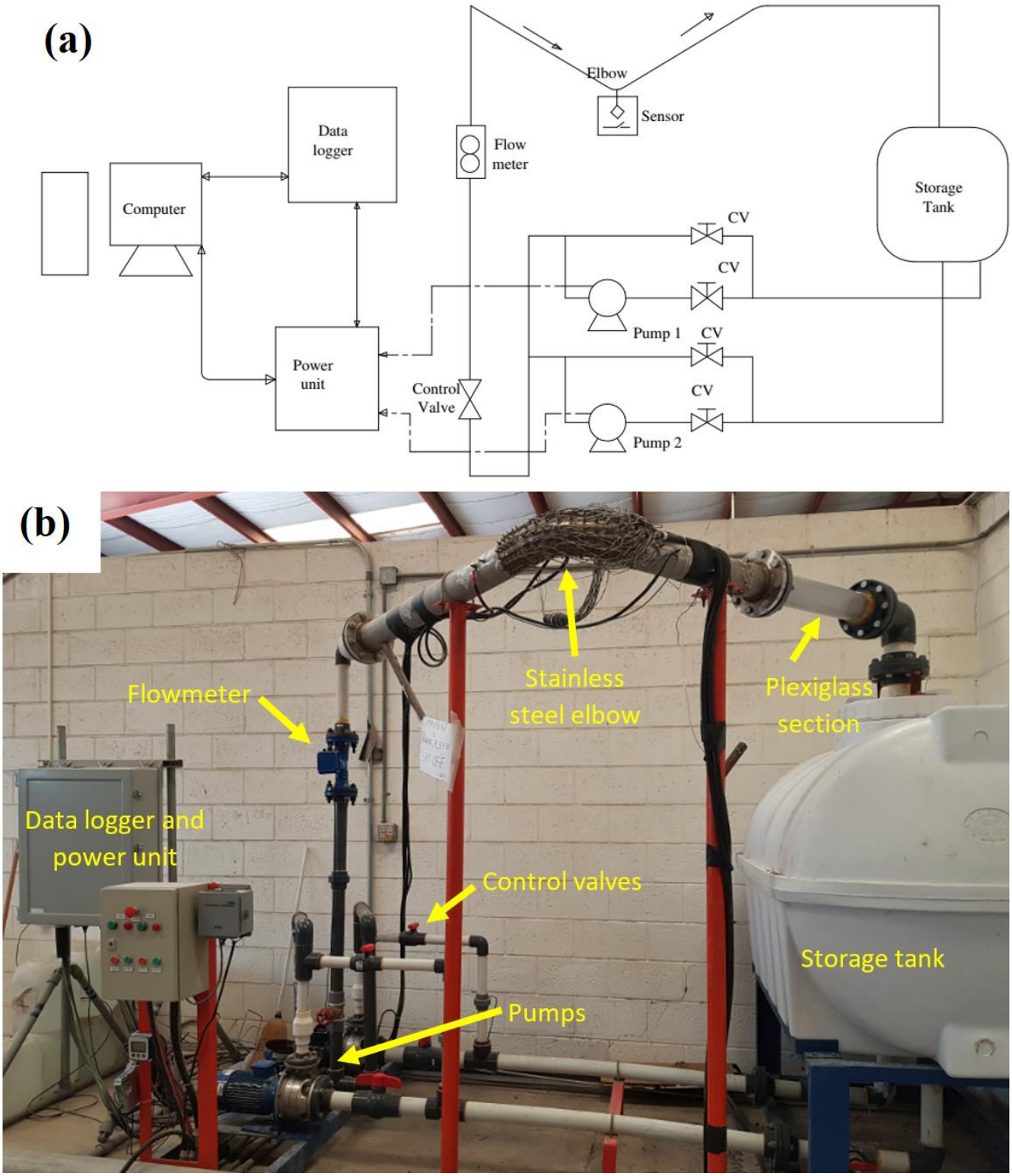

Figure 1. Mini flow loop. (a) Schematic diagram, (b) experimental Set-up.

Table 1. Detailed composition of 316L stainless steel pipe elbow used in the experiment.

Elements	C	Mn	P	S	Cr	Ni	Mo	Si	N	Fe
Wt.% Compositions	0.030	2.000	0.045	0.03	16.00–18.00	10.00–14.00	2.000–3.000	0.750	0.100	balance

Table 2. Physical properties of the working fluid at 25°C.

Fluid	Density (kg/m^3)	Viscosity (cP)
Simulated sea water (35 ppt)	1023.1	1.05

The effect of flowing fluid on the formation of scale in the elbow was monitored and studied with the aid of UT gauge, endoscope camera for visual assessment, and microscopic and spectroscopic equipment at the end of six-month continuous operation period. Change in pipe temperature was also observed and was attributed to the working fluid heat conduction due to heat build-up in the pumps and ambient conditions in the summer season.

3. Results and Discussion

Although the experiment was initially intended to observe the corrosion rate in stainless steel elbow, there was an appreciable and unanticipated increase in wall thickness at the end of the six-month operation period of the loop, as measured using UT gauge. This encouraged the removal of the elbow section to examine the cause of this anomaly. However, owing to the difficulty encountered in visualizing the deposited layer with naked eyes, an endoscope camera with built-in LED lights was employed. Consequently, a scale deposit was found responsible for the increment in wall thickness. This scale deposition was extracted and studied using spectroscopic techniques, namely SEM-EDS, FT-IR, XRD, and XRF. High-pressure washer (Kärcher K2) was used for cleaning the scale deposits to re-measure the wall thickness for assessment of corrosion. In what follows, the reader will find a detailed discussion and results obtained from the above mentioned intrusive and non-intrusive analysis methods.

3.1. Water quality analysis

For insight about the composition of the prepared simulated seawater run through the system, a detailed physical and chemical analysis was conducted on the saline water samples by chemical instruments. A number of parameters such as electrical conductivity (*EC*), total dissolved solids (*TDS*), and metal ions such as Ca, Cu, Zn, Mg, Na, K, Fe, Cd, Pb, and Cr were tested. The composition of the solution obtained from this analysis is shown in Table 3.

Table 3 shows a high value of *TDS* which could deteriorate the elbow pipe by deposition of solids. The Salinity of the saline solution clearly mirror the salinity of a sea water needed for this study. High value of sodium and chlorine in the analysis indicated that saline solution is mainly a solution of sodium chloride.

Table 3. Quality analysis result of saline solution.

Serial No.	Item	Unit	Result
1	*EC*	µS/cm	54.79
2	*TDS* (ppm)	mg/L	35065.60
3	Salinity	‰ (ppt)	35.07
4	Fluoride	mg/L	0.21
5	Bromide	mg/L	181.38
6	Bromate	mg/L	4.34
7	Chloride	mg/L	24852.89
8	Nitrite	mg/L	<0.25
9	Nitrate	mg/L	4.35
10	Sulfate	mg/L	1319.55
11	Ca	mg/L	290.73
12	K	mg/L	56.75
13	Mg	mg/L	93.56
14	Na	mg/L	13289.30
15	Zn	mg/L	0.64

3.2. UT measurements

To ensure that subsequent wall-thickness measurements are taken on the same points, the elbow section was mapped in a matrix layout with 16 columns and 7 rows. UT gauge was used to measure the thickness on these 112 points (16×7) externally before the experiment to collect baseline or reference wall thickness, after the experiment to assess the deposition of scale, and after cleaning for wall loss measurement. These are shown in figure 2 as 3D color maps, where the scale is kept the same to show a comparison of wall thickness change. As seen in the figure, the collected data revealed about 3% increase in the wall thickness on average and a maximum increase of roughly 13%. This increment was due to the scale deposition on the elbow's internal wall.

Wall thickness data collected after a thorough cleaning with the high-pressure washer and distilled water was also compared with the baseline, revealing an average of 2.6% and a maximum 14% decrease. These measurements and observations are in conformance with the results reported in the literature [39–41], that wall thinning are severe at the bend compared with other sections of the pipe owing to sudden changes in the flow direction and velocities [36, 37]. Wall thickness distribution at the center of the matrix outlay (Row 4) was plotted in Figure 3 The reduction in the wall thickness at the mapped elbow section is not the same due to non-uniformity of the pipe's internal wall thickness and more impingement

at the main elbow due to flow redirection. The chemical reaction between the simulated sea water and the pipe walls brings about corrosion manifested by reduced wall thickness and scale formation [38–42]. The nucleation of scale on the internal wall prevents further corrosion into the pipe; however, its accumulation could lead to blockage. If proper monitoring is not in place, pipeline blockage can interrupt oil production and disrupt fuel delivery by pipeline [43–45].

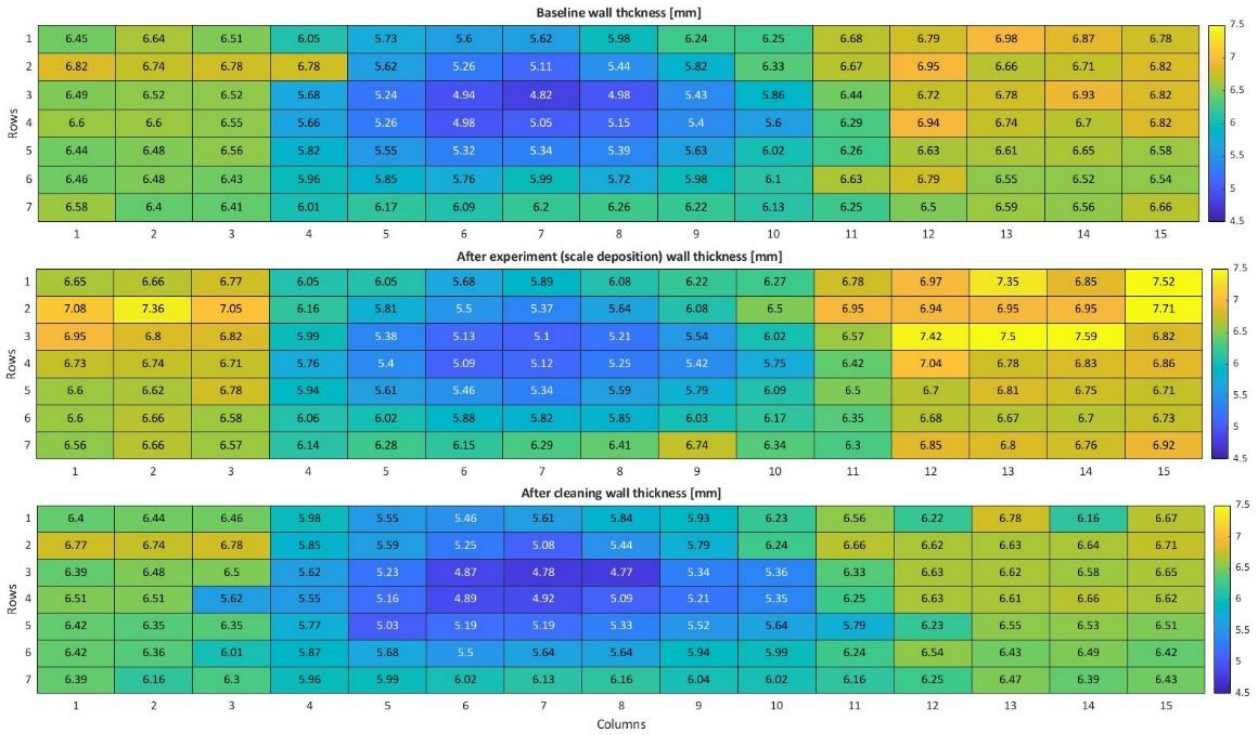

Figure 2. Pipe wall thickness color map before the experiment, after the experiment and after cleaning.

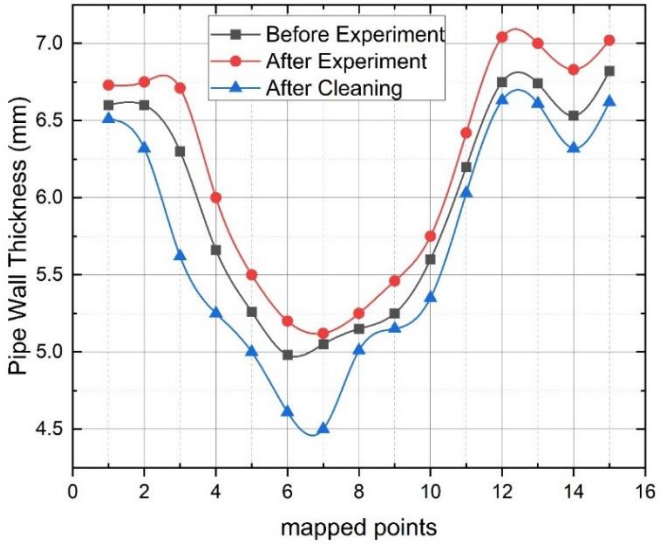

Figure 3. Pipe wall thickness distribution at the elbow section of the pipe.

It can be seen from the graph that the elbow section thickness increases after six months of exposure to the solution as a result of the scale deposit on the elbow wall. The wall thickness reduced below the baseline after cleaning, with maximum thickness loss recorded around the middle of the elbow section (Row 4, point 7) of the pipe, corresponding to the extrados of the bend.

3.3. Visual inspection

The change in pipe wall appearance due to corrosion was expected. However, an increase in wall thickness, as mentioned before, was not. This lead to the idea of visual inspection of elbow's inside wall using an endoscope camera. Figure 4 depicts the images thus obtained after the experiment.

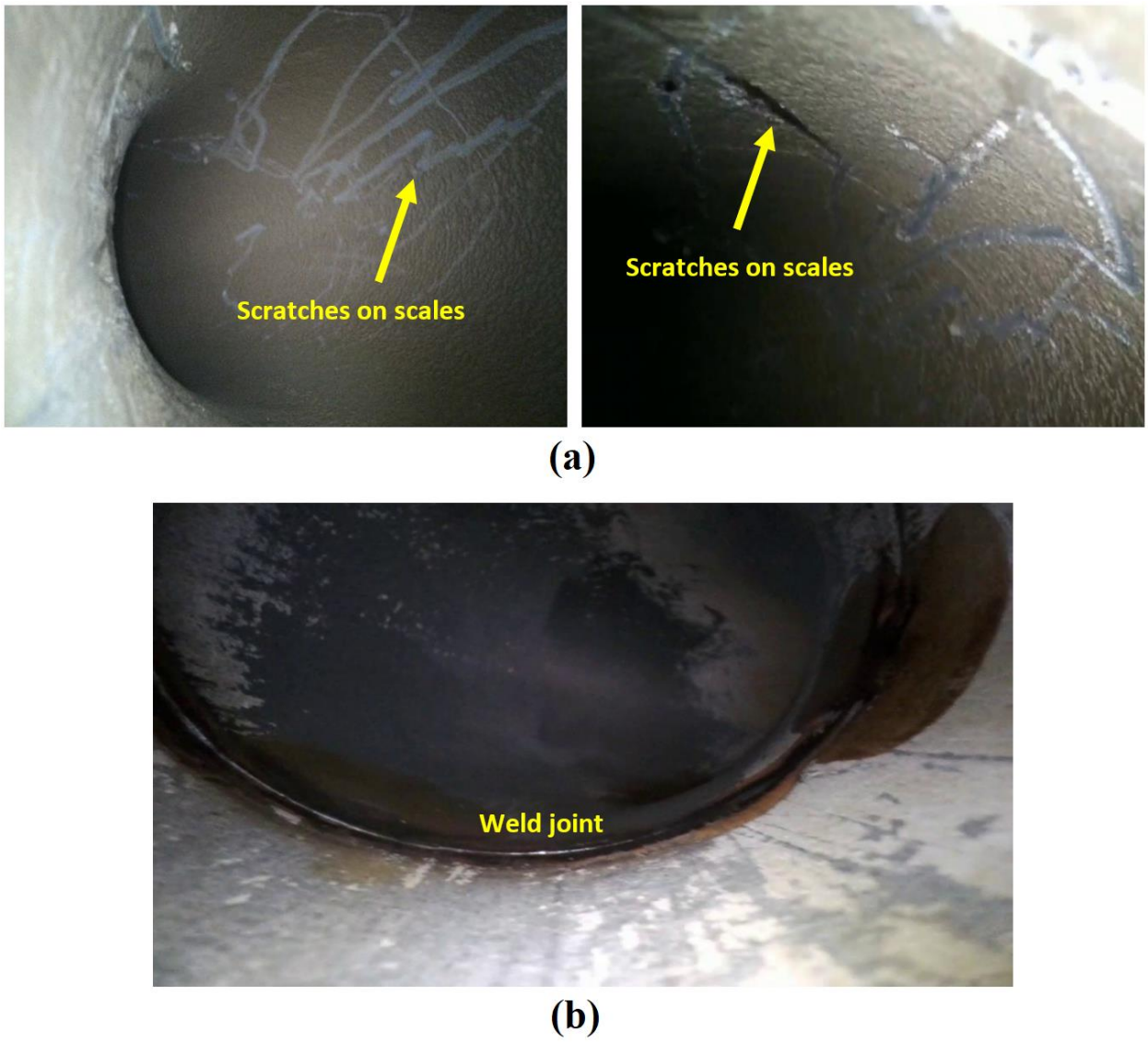

Figure 4. Photograph of elbow internal wall visualized with an endoscope camera. (a) Before cleaning; (b) after cleaning.

Figure 4(a) shows the elbow wall surface scratched with an object during inspection, giving an idea about the scale thickness. It can be seen that the observed increase in the pipe thickness resulted from the scale deposition on the pipe internal wall. The pipe's internal surface after a thorough cleaning with high-pressure washer cleared majority deposits as shown in Figure 4(b). The figure also shows that the corrosion is more pronounced at weld joining the elbow section with the inlet and exit arms as a result of high stresses experiment at the fusion zone of the weld. Also, the cyclic heating and cooling associated with the welding process affects the microstructure and surface composition of the joint and adjacent base metal. The material of the filler metal used for welding might be different from that of the pipe; dissimilar metals at the fusion zone can lead to galvanic corrosion [46]. The accumulation of scale deposit is more pronounced at the main elbow section. It might lead to blockage if proper mitigation techniques is not in place. The same behavior is experienced for corrosion at the elbow joint [47, 48].

3.4. Microstructural characterization of the deposited scale sample

Samples of the scale deposit were collected from the pipe and characterized using various spectroscopic equipment to capture the morphology and composition of the extracted deposit sample. Specifically, SEM: JSM-6610, Joel coupled with EDS, XRD: Ultima IV, Rigaku Co., XRF: Xenemetrix, EX-6600 series, and FT-IR 8400S, Shimadzu Co. were used. In what follows, the analysis results of these methods are discussed.

3.4.1. Scanning Electron Microscopy (SEM)

Figure 5 shows the SEM micrograph of the extracted samples. Morphology of the scale deposit collected from plate heat exchanger by author name [49] (Figure 5a) is compared with the micrograph obtained from this work (Figure 5b). The morphologies of the scale particles are agglomerates of elongated elementary crystallites (rod-like) with an average diameter of about 200 nm and length of the order 1 μm.

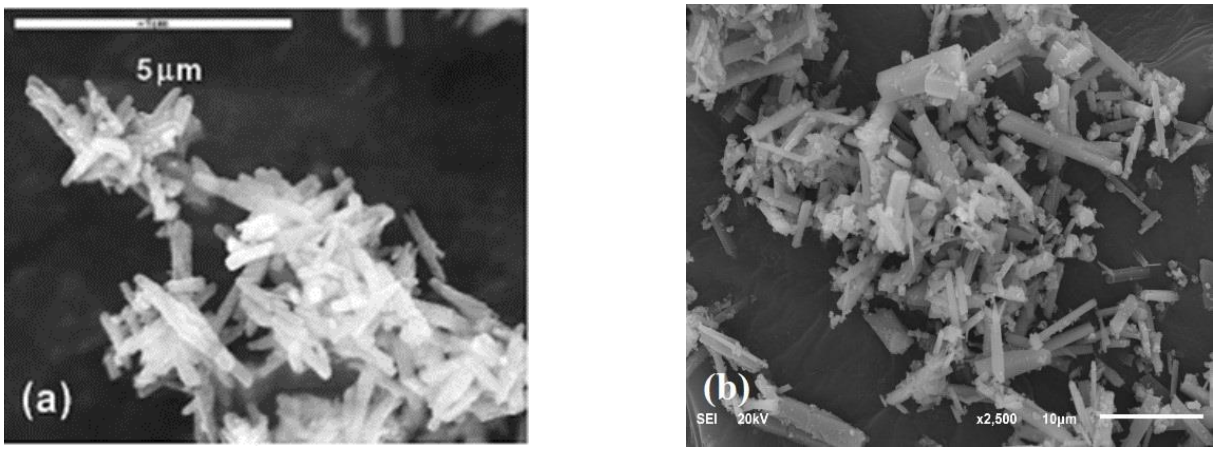

Figure 5. SEM Micrograph of Scale deposit samples. (a) Aragonite particle from the literature [49]; (b) Extracted from stainless steel elbow in this experiment.

In addition to the comparison with the literature, SEM micrograph observed at various sites on the deposit sample is shown in Figure 6(a–d). This is employed to visualize the shape of a fully grown crystal on a layer of agglomerated deposits. The morphology of the scale deposit shows a rod or needle-like crystal typical of crystalline material. The crystallization of $CaCO_3$ causes aggregation of the particles which gives rise to different morphologies depending on the conditions. In the literature, it has been reported that $CaCO_3$ precipitates to give three different types of crystal structures which include aragonite, calcite, and vaterite [50].

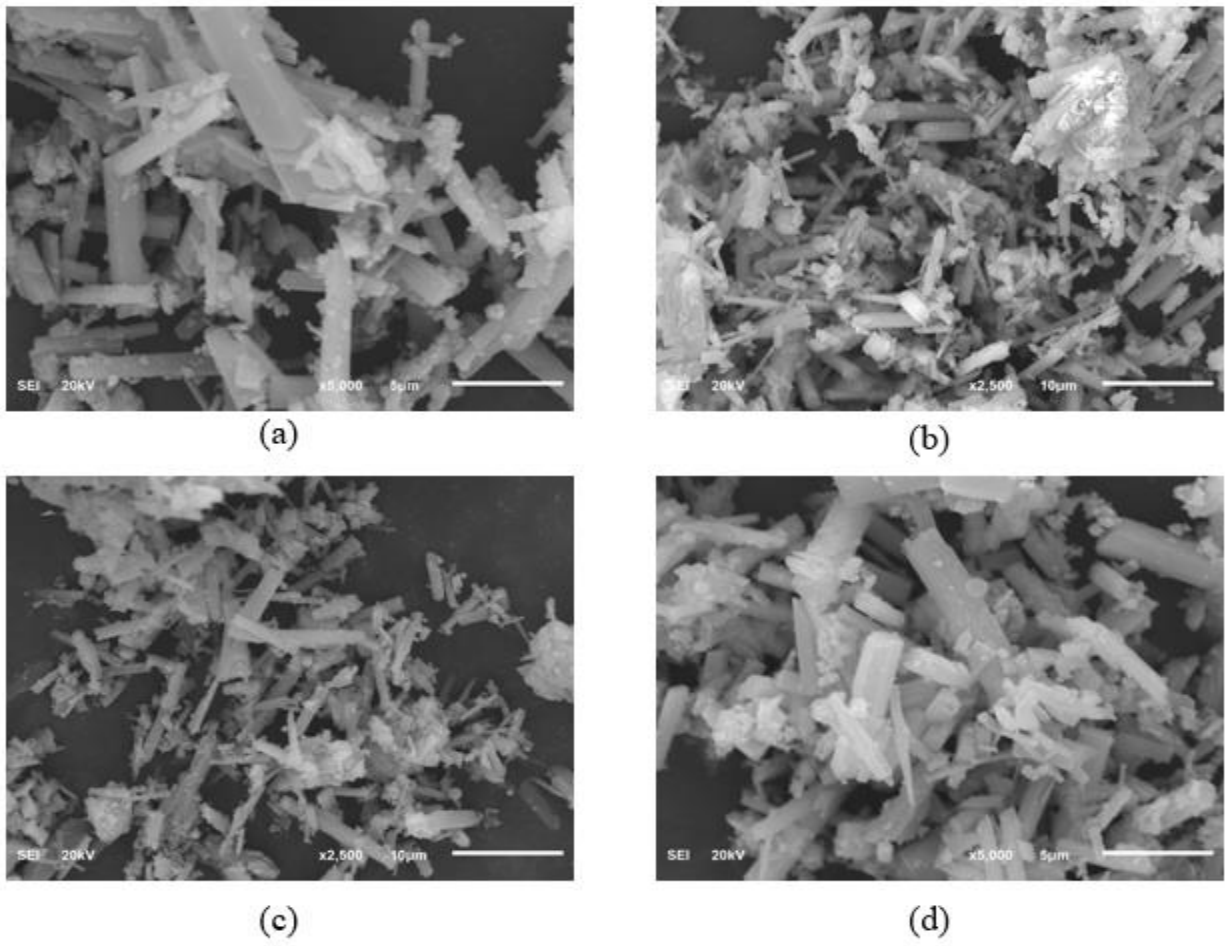

Figure 6. SEM analysis of scale deposit sample morphology at different magnifications. (a) X5000, 5 μm; (b) X2500, 10 μm; (c) X2500, 10 μm (observed at different site); (d) X5000, 5 μm (observed at different site).

The extracted scale sample is aragonite, based on the morphology presented in the literatures. This is confirmed with other spectroscopic equipment, as reported below.

3.4.2. Energy Dispersive X-ray Spectroscopy (EDS)

The elemental composition of the extracted scale deposit sample was qualitatively identified using EDS (Figure 7). The analysis showed that it is composed of Ca, C, O, Au, Na, Zn, Cl,

Si, Fe, and Cu. The highest peaks in the figure correspond to Ca, C, and O from $CaCO_3$. Oxygen was derived from the corrosion product and some deposits. Si was mainly from the mineral deposits and steel composition. Na and Cl were derived from NaCl PDV salt used to prepare the saline solution. Ca detected on the scale was judged to be a mineral deposit from the saline solution. The sources of Cu and Zn can be attributed to the dirt or foreign particles in the saline solution. Fe was found in low concentration because the material of the elbow (316L stainless steel) has a very high corrosion resistance.

EDS is not capable of detecting hydrogen [45–46]. This prompted the characterization of the extracted sample with other spectroscopic equipment. It should be noted that the presence of Au in the profile is because of the sputter coating of the sample holder surface with gold.

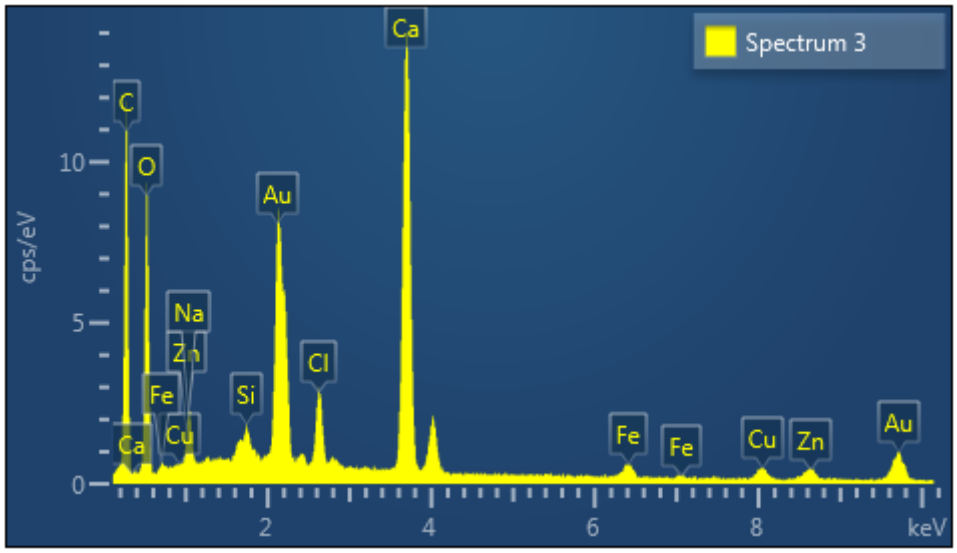

Figure 7. EDS profile of the extracted scale deposit sample from the elbow. Note: cps – counts per second; eV – electron volts.

3.4.3. X-Ray Fluorescence (XRF)

XRF scan on the extracted scale deposit sample revealed the elements (and their oxide states) which could not be captured with EDS analysis; the analysis indicated Ca as the principal element as shown in Figure 8. This is then followed by Oxygen, Iron, Chlorine, and Zinc, while Chromium, Nickel, Manganese, and Copper are present in trace amounts which can mainly be attributed to stainless steel, as shown in Table 4. The deposition of corroded pipe material is indicated with the presence of 7.55% Iron oxide and a trace amount of Cr, Mn, Zn, and Ni from the chemical composition of stainless steel. Cr is one of the main constituent elements of stainless steel responsible for improving its corrosion resistance in oxidizing media [53]. A significant amount of Zinc (4.57%) is from the main composition of saline water run through the loop as confirmed by the water quality analysis in Table 3.

Table 4. XRF Quantitative Chemical Analysis of the deposit Sample (weight %).

Compound	Weight (%)
Calcium oxide (CaO)	81.96
Iron oxide (FeO)	7.55
Zinc oxide (ZnO)	4.57
Chromium oxide (Cr_2O_3)	0.52
Nickel oxide (NiO)	0.25
Manganese oxide (MnO)	0.19

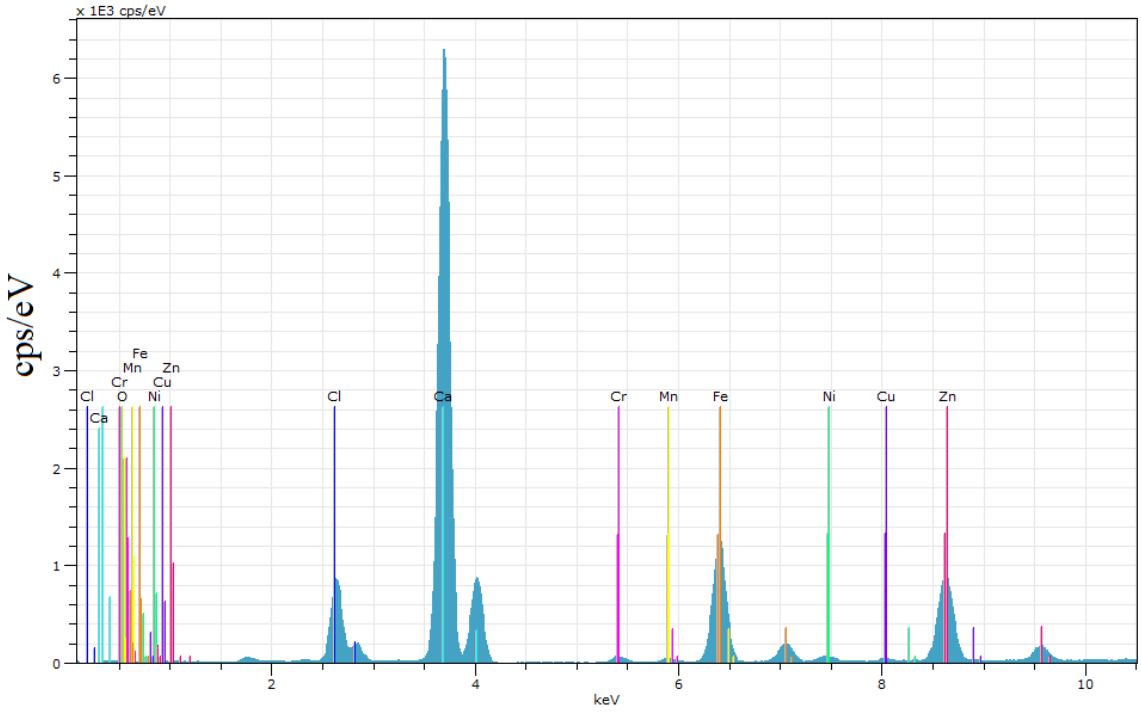

Figure 8. XRF scan showing element not capture by EDS in the scale deposit sample.

3.4.4. X-Ray Diffraction (XRD)

The diffraction pattern of the scale deposit is shown in Figure 9. XRD helps to establish sample's crystalline structure. The observed narrow peaks in the diffractogram are indicative of a high crystallinity related to $CaCO_3$ in the aragonite phase. Presence of Calcium Carbonate can be explained based on the use of tap water in preparation of the saline solution. This is indicative of the hard water, as shown in Equation 1. In addition to this, the saline solution used as working fluid in the experiment is responsible for the crystal formation.

$$Ca^{2+}_{(aq)} + 2HCO^{-}_{3(aq)} \rightarrow CaCO_{3(s)} + H_2O + CO_2 \quad (1)$$

The working fluid run through this system gets heated as a result of heat convection from the centrifugal pump during the experiment. Owing to this, Ca^{2+} ions react with bicarbonate (HCO_3^-) ions to form insoluble $CaCO_3$ scales on the pipe's internal wall.

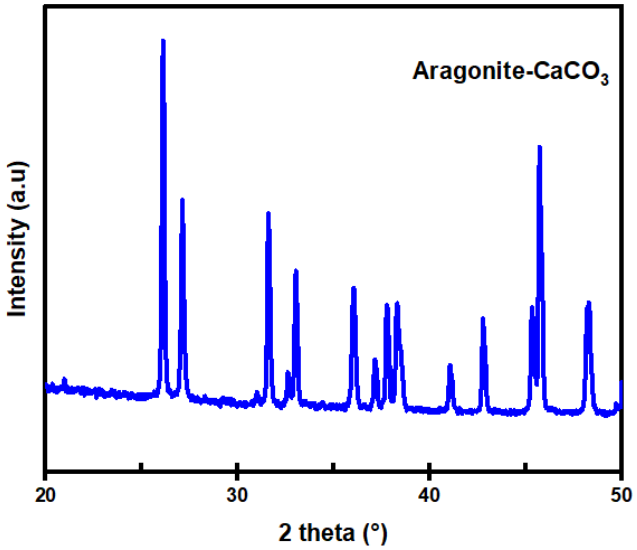

Figure 9. X-ray diffraction spectrum showing the predominant presence of aragonite-$CaCO_3$ in the scale deposit sample.

3.4.5. Fourier Transform Infrared Spectroscopy (FT-IR)

The aragonite polymorph of $CaCO_3$ can easily be identified based on its characteristic peaks in the FT-IR spectrum in Figure 10. The crystals showed distinctive peaks at 709.1, 854.3, and 1486.7 cm^{-1} due to the C–O stretching and bending modes. The peaks at 709.1 and 1486.7 cm^{-1} are attributed to the C–O bond out-of-plane bending and stretching vibrations, respectively. The aragonite crystal is further confirmed by the characteristic vibrational band at 854.3 cm^{-1} which is assigned to the C–O in-plane bending motion [54].

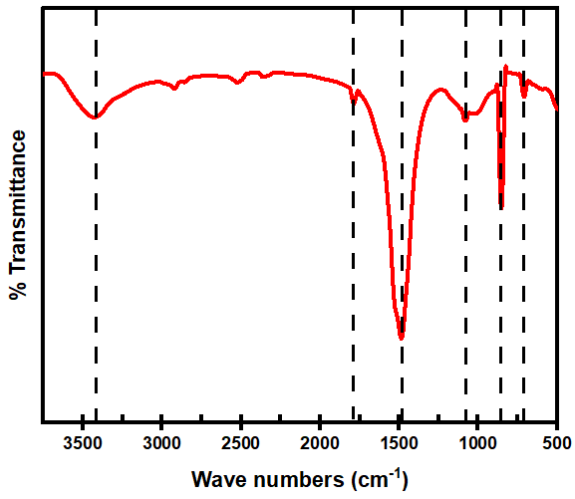

Figure 10. FTIR Spectrum of the extracted scale deposit sample.

Conclusion

In this study, ultrasonic tool, visual inspection using borescope camera, microscopic and spectroscopic equipment were used to investigate the corrosion and scale formation on 316L stainless steel elbow in simulated seawater. The simulated seawater was continuously running through a mini-flow loop system consisting of a stainless-steel elbow pipe for six months at a flow rate of 70 m^3/hr. The ultrasonic thickness gauge was used to measure the elbow wall thickness before and after experiment, and after cleaning. Spectroscopic equipment (SEM-EDS, XRD, XRF, and FT-IR) were used to characterize the scale sample collected from elbow surface.

The major findings from the study are outlined as follows:

1. The scale deposition in the stainless-steel elbow was observed as wall-thickness increase by the ultrasonic equipment. Specifically, about 3% increase in the wall thickness on average and a maximum increase of roughly 13% was noted, as compared with the nominal baseline wall thickness of the pipe.
2. After cleaning the scale, an average of 2.6% and a maximum 14% decrease was observed in the wall thickness, compared with the baseline. This reduction was due to corrosion.
3. Visual inspection with a borescope camera before cleaning, revealed that the increase in wall thickness observed with ultrasonic tools was indeed due to the scale deposition.
4. SEM micrograph of the extracted scale sample showed a rod or needle-like crystal typical of an aragonite particle. This was further confirmed by XRD and FT-IR spectra.
5. EDS and XRF analysis indicated that the extracted scale deposit was composed of Ca, C, O, Na, Zn, Cl, Si, Fe, Cu, Ni, Cr, Mn, and oxide states of some elements (Ca, Fe, Cr, Ni, Mn). Ca, C and O elements were from $CaCO_3$ contained in the simulated seawater, Na and Cl were from the PDV salt used to prepare the solution, Ni, Cr, Mn, Si, Fe were due to the degradation of stainless steel, source of Cu is attributed to the dirt or foreign material in the solution. Furthermore, oxidation of Fe and the formation of oxide film confirm the deposition of corrosion on the pipe's internal wall.

Acknowledgements

The authors would like to acknowledge the support provided by the Deanship of Research at King Fahd University of Petroleum and Minerals (KFUPM), Saudi Arabia for funding this work through Project No. SR191004.

References

1. F.H. Almutairi and D.R. Davies, Detection of scale deposition using distributed temperature sensing, SPE International Oilfield Scale Conference, 2008. doi: 10.2118/113595-MS
2. A. Khormali, D.G. Petrakov and R.N. Moghaddam, Study of adsorption/desorption properties of a new scale inhibitor package to prevent calcium carbonate formation

during water injection in oil reservoirs, *J. Pet. Sci. Eng*., 2017, **153**, 257–267. doi: 10.1016/j.petrol.2017.04.008
3. S. Naseri, J. Moghadasi and M. Jamialahmadi, Effect of temperature and calcium ion concentration on permeability reduction due to composite barium and calcium sulfate precipitation in porous media, *J. Nat. Gas Sci. Eng*., 2015, **22**, 299–312. doi: 10.1016/j.jngse.2014.12.007
4. T. Yi, Z. Jin, X. Chuan-Li and W. Wei-Ying, A Bohai Sea SZ36-1 oil field formation scaling experimental study and scale inhibitor optimization, *Pet. Sci. Technol*., 2014, **32**, no. 20, 2512–2519. doi: 10.1080/10916466.2011.584098
5. J. Macadam and S.A. Parsons, Calcium carbonate scale control, effect of material and inhibitors, *Water Sci. Technol*., 2004, **49**, no. 2, 153–159. doi: 10.2166/wst.2004.0112
6. J. De Baat Doelman, Controlling scale deposition and industrial fouling, *Water Eng. Manage*., 2001, **148**, 19–21.
7. B. Senthilmurugan, B. Ghosh and S. Sanker, High performance maleic acid based oil well scale inhibitors – development and comparative evaluation, *J. Ind. Eng. Chem*., 2011, **17**, no. 3, 415–420. doi: 10.1016/j.jiec.2010.10.032
8. X.L. Wang, C. Zhang and P. Ouyang, The possibility of separating saccharides from a NaCl solution by using nanofiltration in diafiltration mode, *J. Membr. Sci*., 2002, **204**, no. 1–2, 271–281. doi: 10.1016/S0376-7388(02)00050-9
9. Z. Amjad and J. Hooley, Influence of polyelectrolytes on the crystal growth of calcium sulfate dihydrate, *J. Colloid Interface Sci*., 1986, **111**, no. 2, 496–503. doi: 10.1016/0021-9797(86)90052-4
10. L. Sanders, X. Hu, E. Mavredaki, V. Eroini, R. Barker and A. Neville, Assessment of combined scale/corrosion inhibitors – A combined jar test/bubble cell, *J. Pet. Sci. Eng*., 2014, **118**, 126–39. doi: 10.1016/j.petrol.2014.04.008
11. M. El-Said, M. Ramzi and T. Abdel-Moghny, Analysis of oilfield waters by ion chromatography to determine the composition of scale deposition, *Desalination*, 2009, **249**, 748–756. doi: 10.1016/j.desal.2008.12.061
12. A. Quddus and L.M. Al-Hadrami, Influence of solution hydrodynamics on the deposition of $CaSO_4$ scale on aluminum, *J. Thermophys. Heat Transfer*, 2011, **25**, no. 1,112–118. doi: 10.2514/1.44865
13. H. Müller-Steinhagen, *Heat exchanger fouling: mitigation and cleaning techniques*, Dresden International University, Germany, 2000.
14. M. Crabtree, D. Eslinger, P. Fletcher, M. Miller, A. Johnson and G. King, Fighting scale – removal and prevention, *Oilfield Rev*., 1999, **11**, 30–45.
15. M.M. Vazirian, T.V.J. Charpentier, M. de Oliveira Penna and A. Neville, Surface inorganic scale formation in oil and gas industry: As adhesion and deposition processes, *J. Pet. Sci. Eng*., 2016, **137**, 22–32. doi: 10.1016/j.petrol.2015.11.005
16. O. Vazquez, I Fursov and E. Mackay Automatic optimization of oilfield scale inhibitor squeeze treatment designs, *J. Pet. Sci. Eng*., 2016, **147**, 302–307. doi: 10.1016/j.petrol.2016.06.025

17. O.J. Vetter, Oilfield Scale – Can We Handle It?, *J. Pet. Technol*., 1976, **28**, no. 12, 1402–1408. doi: 10.2118/5879-PA
18. R.A. Kippersund, P. Lunde and K.E. Frøysa, Hydrate deposit detection in pipes using ultrasonic guided waves, Proceedings of the 34th Scandinavian Symposium on Physical Acoustics, 2011.
19. J.K. Smith, M. Yuan, U.T. Lopez, M. Means and J.L. Przybylinski, Real-time and in-situ detection of calcium carbonate scale in a West Texas oil field, *SPE Prod. Facil*., 2004, **19**, no. 2, 94–99. doi: 10.2118/87376-PA
20. J.P. Poyet, G. Ségéral and E. Toskey, Real-time method for the detection and characterization of scale, International Symposium on Oilfield Scale, 2002. doi: 10.2118/74659-MS
21. M. Jelbuldina, H. Younes, I. Saadat, L. Tizani, S. Sofela and A.Al Ghaferi, Fabrication and design of CNTs inkjet-printed based micro FET sensor for sodium chloride scale detection in oil field, *Sens. Actuators, A*, 2017, **263**, 349–356. doi: 10.1016/j.sna.2017.06.035
22. P. Rostron, Critical Review of Pipeline Scale Measurement Technologies, *Indian J. Sci. Technol*., 2018, **11**, no. 17, 1–18. doi: 10.17485/ijst/2018/v11i17/121459
23. D.F. Oliveira, R.S. Santos, A.S. Machado, ASS Silva, M.J. Anjos and R.T. Lopes, Characterization of scale deposition in oil pipelines through X-Ray Microfluorescence and X-Ray microtomography, *Appl. Radiat. Isot*., 2019, **151**, 247–255. doi: 10.1016/j.apradiso.2019.06.019
24. R.P. Singh Gaur, Genesis and Phase Characterization of Oil-Field Calcium Sulfate Scales, OnePetro, 2019.
25. F. Echeverría, J.G. Castaño, C. Arroyave, G. Peñuela, A. Ramírez and J. Morató, Characterization of Deposits Formed in a Water Distribution System, *Rev. Chil. Ing*., 2009, **17**, 275–281. doi: 10.4067/s0718-33052009000200016
26. Y. Cui, S. Liu, K. Smith, K. Yu, H. Hu, Y. Li and W. Jiang, Characterization of corrosion scale formed on stainless steel delivery pipe for reclaimed water treatment, *Water Res*., 2016, **88**, 816–825. doi: 10.1016/j.watres.2015.11.021
27. C.P. East, W.O.S. Doherty, C.M. Fellows and H. Yu, Characterization of sugar juice heat exchanger tube deposit, *Surf. Interface Anal*., 2011, **43**, no. 9, 1231–1239. doi: 10.1002/sia.3704
28. A.O. Olufade and C.J. Simonson, Characterization of the Evolution of Crystallization Fouling in Membranes, *ACS Omega*, 2018, **3**, no. 12, 17188–17198. doi: 10.1021/acsomega.8b01058
29. Z.F. Yin, W.Z. Zhao, Y.R. Feng and S.D. Zhu, Characterisation of CO_2 corrosion scale in simulated solution with Cl^- ion under turbulent flow conditions, *Corros. Eng. Sci. Technol*., 2009, **44**, no. 6, 453–461. doi: 10.1179/174327808X303482
30. C. Ding, K. Gao and C. Chen, Effect of Ca^{2+} on CO_2 corrosion properties of X65 pipeline steel, *Int. J. Miner., Metall. Mater*., 2009, **16**, no. 6, 661–666.

31. L.M. Tavares, E.M. da Costa, J.J. de O. Andrade, R. Hubler and B. Huet, Effect of calcium carbonate on low carbon steel corrosion behavior in Saline CO_2 high pressure environmentals, *Appl. Surf. Sci.*, 2015, **359**, 143–152. doi: 10.1016/j.apsusc.2015.10.075
32. N. Sridhar, D.S. Dunn, A.M. Anderko, M.M. Lencka and H.U. Schutt, Effects of water and gas compositions on the internal corrosion of gas pipelines – modeling and experimental studies, *Corrosion*, 2001, **57**, no. 3, 221–235. doi: 10.5006/1.3290347
33. G. Zhao, X. Lu, J. Xiang and Y. Han, Formation Characteristic of CO_2 Corrosion Product Layer of PlIO Steel Investigated by SEM and Electrochemical Techniques, J. *Iron Steel Res. Int.*, 2009, **16**, 89–94. doi: 10.1016/S1006-706X(09)60067-4
34. M. El-Gammal, H. Mazhar, J.S. Cotton, C. Shefski, J. Pietralik and C.Y. Ching. The hydrodynamic effects of single-phase flow on flow accelerated corrosion in a 90-degree elbow, *Nucl. Eng. Des.*, 2010, **240**, no. 6, 1589–1598. doi: 10.1016/j.nucengdes.2009.12.005
35. W.H. Ahmed, M.M. Bello, M. El Nakla, A. Al Sarkhi and H.M. Badr, Experimental investigation of flow accelerated corrosion under two-phase flow conditions, *Nucl. Eng. Des.*, 2014, **267**, 34–43. doi: 10.1016/j.nucengdes.2013.11.073
36. A.K. Hamzat, I.A. Adediran, L.M. Alhems and M. Riaz, Investigation of Corrosion Rate of Mild Steel in Fruit Juice Environment Using Factorial Experimental Design, *Int. J. Corros.*, 2020, **2020**. doi: 10.1155/2020/5060817
37. A.M. Memon, U.T. Salman, A.K. Hamzat and L.M. Al Hems, Neural network method for the modeling of SS 316L elbow corrosion based on electric field mapping, *Corros. Rev.*, 2022, **40**, no. 4. doi: 10.1515/corrrev-2021-0057
38. S.A. Habeeb and H.A. Almashhadani, Synthesis of polysulfanilamide by electro polymerization and its corrosion protective properties on 316L stainless steel in 0.2 M HCl, *Int. J. Corros. Scale Inhib.*, 2022, **11**, no. 2, 621–632. doi: 10.17675/2305-6894-2022-11-2-11
39. V. Kechin, E. Lyublinski and A. Kireev, The influence of technological factors on electrochemical characteristics of cast magnesium cathodic protective elements, *Int. J. Corros. Scale Inhib.*, 2019, **8**, no. 3, 600–612. doi: 10.17675/2305-6894-2019-8-3-10
40. V.N. Dorofeeva, A.I. Shcherbakov, I.G. Korosteleva, I.V. Kasatkina, L.P. Kornienko and V.E. Kasatkin, Pitting corrosion of AISI 420 stainless steel in detergent–disinfectant solutions based on Catamine AB. Inhibiting effect of sulfate ions, *Int. J. Corros. Scale Inhib.*, 2022, **11**, no. 2, 659–665. doi: 10.17675/2305-6894-2022-11-2-14
41. V.E. Kasatkin, V.N. Dorofeeva, I.V. Kasatkina, I.G. Korosteleva, L.P. Kornienko, N.N. Andreev, I.A. Gedvillo and A.S. Zhmakina, Ascorbic acid as a corrosion inhibitor of steel in chloride-containing solutions of calcium hydroxide, *Int. J. Corros. Scale Inhib.*, 2022, **11**, no. 2, 727–751. doi: 10.17675/2305-6894-2022-11-2-19
42. V.I. Vigdorovich, L.E. Tsygankova, L.G. Knyazeva, A.V. Dorokhov, A.N. Dorokhova and M.V. Vigdorowitsch, Suppression of local corrosion of steel, brass and copper with IFKhAN-114 volatile inhibitor, *Int. J. Corros. Scale Inhib.*, 2019, **8**, no. 1, 42–49. doi: 10.17675/2305-6894-2019-8-1-4

43. F. Zanotto, A. Frignani, A. Balbo, V. Grassi and C. Monticelli, Influence of $CeAlO_3$ nanoparticles on the performances of silane coatings for AZ31 alloy, *Int. J. Corros. Scale Inhib.*, 2019, **8**, no. 4, 954–973. doi: 10.17675/2305-6894-2019-8-4-10
44. M. Sieber, S. Lautner and F. Faßbender, Test method and device for evaluation of volatile corrosion inhibitors, *Int. J. Corros. Scale Inhib.*, 2019, **8**, no. 4, 908–925. doi: 10.17675/2305-6894-2019-8-4-7
45. Ahmed S. Alshamsi, Afra G. AlBlooshi, Almaha S. Alshamsi, Asma Y. Alkaabi, Yasmeen S. Elnasiri and Mouza M. Aldhaheri, The effects of surface roughness, chloride, and molybdate on the corrosion behavior of iron in bicarbonate/carbonate solutions, *Int. J. Corros. Scale Inhib.*, 2019, **8**, no. 4, 835–849. doi: 10.17675/2305-6894-2019-8-4-4
46. U.K. Chatterjee, S.K. Bose and S.K. Roy, *Environmental degradation of metals*, Corrosion technology series/14, CRC Press, 2001, 510. doi: 10.1201/9781482292244
47. N.A. Vetlugin and N.A. Polyakov, Influence of water-soluble monomers on the corrosion protection ability of chromium coatings obtained from Cr(III)-based solutions, *Int. J. Corros. Scale Inhib.*, 2018, **7**, no. 4, 570–581. doi: 10.17675/2305-6894-2018-7-4-6
48. S.A. Habeeb and H.A. Almashhadani, Synthesis of polysulfanilamide by electro polymerization and its corrosion protective properties on 316L stainless steel in 0.2 M HCl, *Int. J. Corros. Scale Inhib.*, 2022, **11**, no. 2, 621–632. doi: 10.17675/2305-6894-2022-11-2-11
49. N. Andritsos and A.J. Karabelas, Calcium carbonate scaling in a plate heat exchanger in the presence of particles, *Int. J. Heat Mass Transfer*, 2003, **46**, no. 24, 4613–4627. doi: 10.1016/S0017-9310(03)00308-9
50. N. Andritsos, A.J. Karabelas and P.G. Koutsoukos, Morphology and structure of $CaCO_3$ scale layers formed under isothermal flow conditions, *Langmuir*, 1997, **13**, no. 10, 2873–2879. doi: 10.1021/la960960s
51. K. Hristovski, P. Westerhoff and J. Crittenden, An approach for evaluating nanomaterials for use as packed bed adsorber media: A case study of arsenate removal by titanate nanofibers, *J. Hazard. Mater.*, 2008, **156**, no. 1–3, 604–611. doi: 10.1016/j.jhazmat.2007.12.073
52. Y. Song, D. Shan, R. Chen, F. Zhang and E.H. Han, Formation mechanism of phosphate conversion film on Mg–8.8Li alloy, *Corros. Sci.*, 2009, **51**, no. 1, 62–69. doi: 10.1016/j.corsci.2008.10.001
53. Aalco, Stainless Steel: Alloying in Elements Stainless Steel, 2013. https://www.aalco.co.uk/datasheets/Aalco-Metals-Ltd_Stainless-Steel-Alloying-Elements-in-Stainless-Steel_98.pdf.ashx (Accessed on 15 August 2020)
54. N. Koga, D. Kasahara and T. Kimura, Aragonite crystal growth and solid-state aragonite–calcite transformation: A physico–geometrical relationship via thermal dehydration of included water, *Cryst. Growth Des.*, 2013, **13**, no. 5, 2238–2246. doi: 10.1021/cg400350w

♦ ♦ ♦